

Enhanced thermoelectric performance of polycrystalline SnSe by compositing with layered $Ti_3C_2T_x$

Yi Qin

Shaanxi University of Science and Technology

Xiaohan Li

Shaanxi University of Science and Technology

Ting Zhao (✉ zhaoting@sust.edu.cn)

Shaanxi University of Science and Technology

Jianfeng Zhu

Shaanxi University of Science and Technology

Yanling Yang

Shaanxi University of Science and Technology

Meiqian Xie

Shaanxi University of Science and Technology

Research Article

Keywords: polycrystalline SnSe, $Ti_3C_2T_x$, electrostatic self-assembly, thermoelectric properties

Posted Date: June 11th, 2021

DOI: <https://doi.org/10.21203/rs.3.rs-607248/v1>

License:  This work is licensed under a Creative Commons Attribution 4.0 International License.

[Read Full License](#)

Abstract

Thermoelectric materials convert thermal energy into electricity directly. Constructing nanostructured composite architectures can be an effective strategy to develop thermoelectric performance. SnSe/Ti₃C₂T_x composite materials were synthesized through the electrostatic self-assembly method followed by spark plasma sintering. The interfaces introduced by Ti₃C₂T_x can scatter carriers effectively, thus increasing the Seebeck coefficients (S), finally, a high absolute S value of $\sim 296.2 \mu\text{V K}^{-1}$ was obtained at 773 K. At the same time, the high-density interfaces of SnSe/Ti₃C₂T_x composites enhance the phonon scattering, a low lattice thermal conductivity k_{lat} of $0.54 \text{ W m}^{-1} \text{ K}^{-1}$ was obtained in sample $\omega = 0.1\%$. Benefit from the elevated Seebeck coefficient and decreased thermal conductivity, a ZT of 0.1 was obtained in sample $\omega = 0.1\%$ at 773 K along the pressing direction, compared with the pure SnSe, the thermoelectric performance improved by 68%. This research will provide a new way for the development of the thermoelectric properties of polycrystalline SnSe.

1. Introduction

Thermoelectric materials convert thermal energy into electricity directly while they are independent of moving parts and extremely reliable [1], so they will play a key role in power generation. The property of thermoelectric materials is manifested by the dimensionless figure of merit (ZT), $ZT = (S^2\sigma/\kappa) T$, where S , σ , $S^2\sigma$, κ , and T are the Seebeck coefficient, electrical conductivity, power factor, thermal conductivity, and absolute temperature, respectively [2]. Many efforts have been taken for developing the ZT value [3–5], the ameliorating methods are divided into two classes, one is using doping to enhance the electrical performance of the thermoelectric materials [6–8], and the other is reducing the lattice thermal conductivity by amplifying phonon scattering [9,10]. But because of the coupling relationship between thermal conductivity and electrical conductivity, it is essential to find materials that have intrinsically low thermal conductivity and adjustable electrical conductivity. SnSe is a thermoelectric material that combines these two advantages.

SnSe has a layered orthorhombic crystal structure [11], the strong anharmonicity in Sn-Se bonding gives rise to high Grüneisen parameters [12], leading to intrinsically low thermal conductivity. Also, a phase transition from $Pnma$ to $Cmcm$ in SnSe results in the divergence of two overlapped conduction bands, which lessens the band mass and obtains high carrier mobility, thus ZT of 2.8 has been achieved in n-type Br-doped SnSe single crystals [13], which is the highest ZT value reached so far. However, SnSe single crystals are easier to disintegrate and harder to prepare than polycrystalline SnSe, so researchers want to use polycrystalline SnSe in place of SnSe single crystals [14]. Polycrystalline SnSe has poorer thermoelectric performance compared with SnSe single crystals [15], so it is necessary that take measures to improve polycrystalline SnSe thermoelectric performance, now many methods have been adopted to raise its thermoelectric properties, such as carrier concentration control [16], band structure adjustment [17], vacancy engineering [18]. Besides, it's also an effective strategy to introduce a suitable nanoscale second phase into the tin selenide matrix [19].

MXenes are new 2D materials that were firstly prepared by selectively etching MAX phases in 2011 [20]. They exhibit metal-like electrical properties and have graphene-like structures [21]. The excellent electrical properties can improve the electrical performance of the composites and the dimensional graphene-like nanostructure can enhance the phonon scattering and further reduce the thermal conductivity of the composites [22]. MXenes have been used in $\text{Bi}_{0.4}\text{Sb}_{1.6}\text{Te}_3$ to enhance thermoelectric properties, because $\text{Bi}_{0.4}\text{Sb}_{1.6}\text{Te}_3$ and MXenes have different work functions, they will cause band bending and scatter low-energy carriers. In addition, the heterogeneous interfaces between $\text{Bi}_{0.4}\text{Sb}_{1.6}\text{Te}_3$ and MXenes can scatter phonons efficiently to reduced thermal conductivity. Finally, a high average ZT of ≈ 1.23 was achieved in the temperature ranging from 300 to 475 K [5]. Hence, MXenes can be expected to improve the thermoelectric performance of polycrystalline SnSe.

In this study, we prepared SnSe powders and $\text{Ti}_3\text{C}_2\text{T}_x$ (T_x represents O, OH, and F groups). $\text{Ti}_3\text{C}_2\text{T}_x$ is representative of MXenes materials. Because the surface of $\text{Ti}_3\text{C}_2\text{T}_x$ is electronegative [23] and the surface of SnSe powder can be positively charged by adjusting the pH value of SnSe powder dispersion [24], we decided to adopt the electrostatic self-assembly method to prepare SnSe/ $\text{Ti}_3\text{C}_2\text{T}_x$ composites powders. Then the powders were sintered by SPS at 773 K under 50 MPa for 5 min. After that, the thermoelectric properties of the sintered pellets were tested. Due to the addition of $\text{Ti}_3\text{C}_2\text{T}_x$, the thermoelectric properties of the composites are better than those of the pure SnSe, the thermoelectric performance improved by 68% when $\omega = 0.1\%$. This research will provide a new way for the development of the thermoelectric properties of polycrystalline SnSe.

2. Materials And Methods

SnSe/ $\text{Ti}_3\text{C}_2\text{T}_x$ - ω ($\omega = 0, 0.05\%, 0.1\%, 0.2\%$) composites, or SnSe-T- ω were synthesized according to the process in Fig. 1. The $\text{Ti}_3\text{C}_2\text{T}_x$ nanosheets were synthesized by etching Ti_3AlC_2 (11 Technology, 99%) in a mixture solution of 1 g LiF (Aladdin, 99%) and 20 ml hydrochloric acid (9 M) for 24 h at 35 °C. Then the products were washed by several centrifugation cycles of deionized water (DI), followed by an ultrasonic concussion for 60 min. Then the dark green supernatant was carefully collected after centrifugation for 60 min at 3500 rpm. The SnSe powders were synthesized by a simple hydrothermal method.

SnCl_2 (Aladdin, 98.0-103.0%), Se powders (Aladdin, 99.99%), and NaOH (Aladdin, 97%) were dissolved in 50ml deionized water under ultrasonic for 20 min, then the mixture was transferred to a reaction kettle (100 ml) and heated at 463 K for 12 h in an oven. After cooling to room temperature, the black precipitate was collected by centrifugation and thoroughly washed with deionized water several times. Finally, the product was dried at 60 °C for 12 h and collected as powder.

$\text{Ti}_3\text{C}_2\text{T}_x$ and SnSe powders were composited by electrostatic self-assembly. SnSe powders were dispersed into deionized water and the pH value of the solution was adjusted to 2 by adding hydrochloric acid (HCl). The dispersion of $\text{Ti}_3\text{C}_2\text{T}_x$ was added into the SnSe solution with slow stirring, then washing the mixed solution with water and freeze-drying.

SPS was done using SPS-2T-2-MIN (Chen Hua, China) instrument. The dried powders were sintered at 773 K under the pressure of 50 MPa for 5 min. The obtained $\text{SnSe/Ti}_3\text{C}_2\text{T}_x$ bulks were cut along the parallel directions to the pressing for electrical transport property measurements and thermal transport property measurement.

The Seebeck coefficients (S) and electrical conductivities (σ) were measured by a Cryoall CTA-3S instrument system under a helium atmosphere from 300 to 773 K. σ and S were measured in parallel to the pressing direction. The Hall coefficient (R_H) was measured by the Van der Pauw technique with a Hall measurement system (MMR H5000) under $\pm 0.9\text{T}$. Hall carrier density (n_H) was calculated through $n_H = 1/(eR_H)$ and Hall carrier mobility (μ_H) was acquired through $\mu_H = R_H/\rho$. The thermal conductivity (κ) was calculated through the equation: $\kappa = DC_p\rho$, where D , C_p , ρ are thermal diffusivity, specific heat capacity, and density, respectively. D was measured with Netzsch LFA 467, C_p was taken from the ref [15], ρ was measured by Archimedes method.

Crystalline phases were identified by X-ray diffraction analysis (XRD, D/MAX-RA, Rigaku, Japan) with $\text{Cu K}\alpha$ radiation and scanning from 10° to 60° . The sampling interval was $0.02^\circ 2\theta$. The microstructure of samples was investigated by field emission scanning electron microscopy (FEI Verios 460) and HRTEM (FEI Tecnai G2 F20 S-TWIN).

3. Results And Discussion

We firstly prepared $\text{Ti}_3\text{C}_2\text{T}_x$ nanosheets by etching Ti_3AlC_2 [25]. The XRD pattern of the $\text{Ti}_3\text{C}_2\text{T}_x$ nanosheet is shown in Fig. 2(a). The (104) peak at $\approx 38^\circ$ in Ti_3AlC_2 indicates the existence of the Al layer in Ti_3AlC_2 . After etching, the (104) peak was disappeared and the (002) peak shifted to a small angle about 6° , which confirm the elimination of the Al layer and the formation of $\text{Ti}_3\text{C}_2\text{T}_x$ with a large interlayer distance. The scanning electron microscope (SEM) and Atomic Force Microscope (AFM) were used to verify the successful preparation of $\text{Ti}_3\text{C}_2\text{T}_x$ nanosheets. Fig. 2(b) shows that the exfoliated $\text{Ti}_3\text{C}_2\text{T}_x$ nanosheets have a large transverse dimension of about one hundred micrometers, and the nanosheets so thin and flexible that form folds on the surface. Fig. 2(c) shows the AFM pictures of $\text{Ti}_3\text{C}_2\text{T}_x$ nanosheets. The height profile indicates the average thickness of 4 nm, which proves that the prepared $\text{Ti}_3\text{C}_2\text{T}_x$ is two-dimension material.

Then SnSe powders were prepared by the conventional hydrothermal method. The XRD pattern of SnSe is shown in Fig. 3(a). The results are indexed with orthorhombic SnSe (space group $Pnma$, PDF#48-1224), and no peaks indicative of impurities are present. We can know that the synthesized SnSe powders have a particle size of ≈ 400 nm, and there are a few flake-like powders of several micrometers from Fig. 3(b) and (c). The results of Transmission Electron Microscopy (TEM) are shown in Fig. 3(d) and (e). The lattice fringes can be seen clearly from the High-resolution TEM image, the crystal plane spacing between two apparent planes is estimated to be 0.29 nm, which corresponds to the (111) planes of SnSe [26].

The SnSe sheets were mixed with $Ti_3C_2T_x$ nanosheets by an electrostatic self-assembly method. $Ti_3C_2T_x$ nanosheets surface is electronegative due to the preparation process [23], and SnSe sheets can be positively charged by adjusting the pH value of the solution [24]. As shown in Fig. 3(f), the zeta potential values of SnSe and $Ti_3C_2T_x$ show different changing rules with the change of pH. The zeta potential of SnSe changes from positive to negative as the pH changes from 2 to 10, but the zeta potential of $Ti_3C_2T_x$ is negative all the time. When the pH value is adjusted to 2, the zeta potential of SnSe sheets and $Ti_3C_2T_x$ nanosheets are +27 and -12, respectively. Therefore, the two different materials can be adsorbed together by electrostatic force when drop adding $Ti_3C_2T_x$ dispersion into the SnSe aqueous dispersion.

Fig. 4(a) shows the XRD patterns of $Ti_3C_2T_x$ and SnSe/ $Ti_3C_2T_x$ composites. The XRD pattern of $Ti_3C_2T_x$ includes one peak at $2\theta = 6^\circ$, which can be attributable to the (002) reflection with an interlayer distance of 0.5 nm. The diffraction peaks of SnSe/ $Ti_3C_2T_x$ composites prove that the powders of synthesized material are orthorhombic SnSe (space group *Pnma*, PDF#48-1224), and no peaks indicative of impurities are present. It is a pity that the diffraction peak of $Ti_3C_2T_x$ can't be observed, even in the SnSe/ $Ti_3C_2T_x$ -0.2% sample, which means that the amount of $Ti_3C_2T_x$ in the composites is so low that the diffractometer could not pick it up. To determine the presence of $Ti_3C_2T_x$ in the composites, SEM and TEM are adopted.

Fig. 4(b) shows the microstructure of SnSe/ $Ti_3C_2T_x$ -0.2% composites, where the thin $Ti_3C_2T_x$ nanosheets are distributed on the surface of the SnSe sheets and SnSe plates are wrapped by the ultrathin $Ti_3C_2T_x$ nanosheets. TEM image Fig. 4(c) shows that $Ti_3C_2T_x$ nanosheets wrap around the SnSe particles. HRTEM image Fig. 4(d) exhibits the lattice fringes with a spacing of 0.3 nm for the particle which corresponds to the (011) planes of

SnSe. Fig. 4(e) gives the corresponding elemental maps of Sn, Se, Ti, and C, which shows that Sn and Se elements are evenly distributed in the wafer, Ti and C are distributed around the wafer. This confirms that the sheet is SnSe and $Ti_3C_2T_x$ is wrapped on top of the SnSe.

The as-synthesized SnSe/ $Ti_3C_2T_x$ composites powders are sintered by the SPS. The sintered samples all have a good density, which can be confirmed by Table 1.

Table 1 Density of the SnSe/ $Ti_3C_2T_x$ composites. The theoretical density of SnSe is 6.18 g/cm³.

SnSe/ $Ti_3C_2T_x$ - ω	Measured density (g/cm ³)	Relative density (%)
$\omega = 0$	6.12	99.03
$\omega = 0.05\%$	6.08	98.38
$\omega = 0.1\%$	6.08	98.38
$\omega = 0.2\%$	6.06	98.06

Fig. 5 shows the XRD patterns of the sintered pellets along with both the parallel and perpendicular to the pressing direction. The diffraction peaks correspond to orthorhombic SnSe. However, the intensities of the (400) peak are a sharp increase in the XRD pattern

collected perpendicular to the pressing direction (Fig. 5(b)), indicating that strong preferred $\{h00\}$ orientation occurs in the SnSe pellets [27]. Fig. 5(c) and (d) are SEM images of SnSe/Ti₃C₂T_x-0.1% pellets, fractured from different directions. The microstructures of the pellets are composed of microplates, indicating that SnSe powders grew further during the high-temperature SPS process. It can be seen that the sample exhibits a layered structure along the parallel direction and a flat plane structure along the perpendicular direction, indicating an obvious anisotropy in the sintered pellets, which fit well with the XRD patterns in Fig. 5(a) and (b).

Since the performance of SnSe is anisotropic, it is easier to obtain low thermal conductivity in the direction of parallel pressure [28], so the test directions in this paper are all parallel to the pressing direction. The graph of the Seebeck coefficients as a function of temperature is shown in Fig. 6(a), in which the Seebeck coefficients decrease (positive) firstly then increase (negative) as long as the temperature increase.

During the low-temperature stage (< 500 K), the main carriers in the material are holes, so S is positive. Then the temperature continues to increase, the bipolar transport will begin ($500\sim 600$ K), in this case, the S should be explained by p and n -type carriers contribute to S together. Because the n -type carriers are going to provide a negative potential, the Seebeck coefficients will decrease sharply, before the main carriers change from p to n -type, about at 600 K, the drop rate of S goes up, when the contribution of p and n carriers to S is equal, S will be zero and the type of the main carrier changes. And then S will continue to increase in the negative direction as the temperature increases, finally, a high absolute S value of $\sim 296.2 \mu\text{V K}^{-1}$ at 773 K is observed ($\omega = 0.2\%$).

The S of composite Ti₃C₂T_x samples is higher than the pure sample, indicating that interfaces in composites scatter carriers, thus increasing S .

The temperature dependences of σ for SnSe/Ti₃C₂T_x composites are shown in Fig. 6(b), the σ of all samples increases with increasing temperature. When the temperature is below 600 K, the σ growth is slow, this is because there is no significant increase in carrier concentration at this stage. Then, σ increases rapidly at temperatures above 600 K due to the thermal excitation of electrons [29]. This tendency of σ with temperature is common in polycrystalline SnSe [30]. At room temperature, the σ of all samples compositing Ti₃C₂T_x is lower than pure SnSe, because the interfaces between SnSe and Ti₃C₂T_x enhance the scattering of carriers to decreased carrier mobility, which can be evidenced from room temperature Hall measurement in Fig. 6(d). The electron intrinsic excitation becomes the main source of carriers during the high-temperature stage, but the electrical conductivity of the composites still does not

exceed pure SnSe, indicating that the interface in the composites still has a strong scattering effect on the carriers so that decrease σ and enhance S .

Fig. 6(c) shows the temperature dependences of PF for SnSe/Ti₃C₂T_x composites. PF ($S^2\sigma$) is the result of σ and S s calculations. During the low-temperature stage (<600 K), even if there is a change in the main carrier type, there is little effect on the PF due to the low conductivity. Then, as the temperature rises, the conductivity increases sharply, as a result, an optimized PF of 0.74 $\mu\text{W cm}^{-1} \text{K}^{-2}$ at 773 K can be observed when $\omega = 0.2\%$.

The total thermal conductivity k_{tot} and lattice thermal conductivity k_{lat} of all samples in the temperature range from 300 K to 773 K are shown in Fig. 7(b) and (c). We estimate the lattice thermal conductivity through the Wiedemann-Franz Law ($\kappa_{ele} = L\sigma T$). Because L will not change the total thermal conductivity and final ZT , an estimation of L can be made using the SPB model with acoustic phonon scattering, the L is calculated from:

$$L = \left(\frac{k_B}{e} \right)^2 \left(\frac{(r+7/2)F_{r+5/2}(\eta)}{(r+3/2)F_{r+1/2}(\eta)} - \left[\frac{(r+5/2)F_{r+3/2}(\eta)}{(r+3/2)F_{r+1/2}(\eta)} \right]^2 \right) \quad (1)$$

where k_B is the Boltzmann constant, e is the electric charge, r is the scattering rate, and η refers to the reduced Fermi energy, which can be derived from the measured Seebeck coefficients with consideration of acoustic phonon dominated scattering ($r = -1/2$) via the following equation:

$$S = \frac{k_B}{e} \left[\frac{(r+5/2)F_{r+3/2}(\eta)}{(r+3/2)F_{r+1/2}(\eta)} - \eta \right] \quad (2)$$

where $F_x(\eta)$ is Fermi integral:

$$F_x(\eta) = \int_0^\infty \frac{\varepsilon^x}{1 + \exp(\varepsilon - \eta)} d\varepsilon \quad (3)$$

Because the electrical conductivity is so low at a temperature below 600 K, the electronic contribution to the thermal conductivity becomes obvious only above 600 K, which leads to no significant difference between the total thermal conductivity k_{tot} and lattice thermal conductivity k_{lat} . It is noteworthy that the min k_{lat} is obtained in sample $\omega = 0.1\%$ at 773 K (0.54 $\text{W m}^{-1} \text{K}^{-1}$), which is comparable to the values of single-crystal SnSe reported by Wei [31]. This indicates that the interfaces between the SnSe matrix and Ti₃C₂T_x can scatter phonon effectively. But the thermal conductivity of sample $\omega = 0.2\%$ is not lower than that of the pure SnSe, this can be explained for two reasons, one is the Ti₃C₂T_x has a higher thermal

conductivity than SnSe [32], the other is the uneven distribution of $\text{Ti}_3\text{C}_2\text{T}_x$ in SnSe matrix results in a reduced scattering interface.

Fig. 7(d) presents the temperature dependence of the figure-of-merit ZT in the temperature range of 300-773 K. The interfaces introduced by $\text{Ti}_3\text{C}_2\text{T}_x$ can scatter carriers effectively, thus increasing the Seebeck coefficients (S), finally, a high absolute S value of $\sim 296.2 \mu\text{V K}^{-1}$ was obtained at 773 K. At the same time, the high-density interfaces of SnSe/ $\text{Ti}_3\text{C}_2\text{T}_x$ composites enhance the phonon scattering, a low lattice thermal conductivity k_{lat} of $0.54 \text{ W m}^{-1} \text{ K}^{-1}$ was obtained in sample $\omega = 0.1\%$. Because of the lowest k_{lat} in sample $\omega = 0.1\%$, the peak ZT value of 0.1 presents at 773 K in sample $\omega = 0.1\%$. Compared with the pure sample, the performance of the composite sample is indeed improved, but the ZT value is still very low, so measures still need to be taken to improve the conductivity, especially the mobility.

4. Conclusions

In this work, we successfully synthesize SnSe/ $\text{Ti}_3\text{C}_2\text{T}_x$ composites materials by the electrostatic self-assembly method and SPS. Because low energy carriers were filtered by interfaces, a high absolute S value of $\sim 296.2 \mu\text{V K}^{-1}$ was obtained at 773 K. The low k_{lat} of $0.54 \text{ W m}^{-1} \text{ K}^{-1}$ was obtained at 773 K due to the scattering of phonons at the interfaces, therefore, a ZT of 0.1 was obtained in sample $\omega = 0.1\%$ at 773 K along the pressing direction, which improves by 68% compared with the pure SnSe in our research. It's a pity that $\text{Ti}_3\text{C}_2\text{T}_x$ can increase the carrier concentration of SnSe but reduce the mobility, which ultimately fails to achieve the purpose of improving the electrical conductivity, therefore, to obtain a higher ZT value, additional measures should be taken to increase mobility.

Declarations

Acknowledgments

This work was supported by the General Project in Industrial Area of Shaanxi Province (Grant No. 2020GY-281), the Shaanxi Provincial Education Department serves Local Scientific Research Plan (Grant No. 20JC008), the National Natural Science Foundation of China (Grant No. 51702193, 51502165), the Natural Science Foundation of Shaanxi Provincial Department of Education (Grant No. 20JK0525) and the Scientific Research Fund of Shaanxi University of Science & Technology (Grant No. BJ16-20, BJ16-21).

References

[1] Bell L E. Cooling, Heating, Generating Heat with and Recovering Waste Thermoelectric. *Science* 2008, **321**: 1457–1461.

- [2] Tan G, Zhao L D, Kanatzidis M G. Rationally Designing High-Performance Bulk Thermoelectric Materials. *Chem Rev* 2016, **116**: 12123–12149.
- [3] He J, Tritt T M. Advances in thermoelectric materials research: Looking back and moving forward. *Science* 2017, **357**: 559-529.
- [4] Biswas K, He J, Blum I D, *et al.* High-performance bulk thermoelectrics with all-scale hierarchical architectures. *Nature* 2012, **489**: 414–418.
- [5] Lu X, Zhang Q, Liao J, *et al.* High-Efficiency Thermoelectric Power Generation Enabled by Homogeneous Incorporation of MXene in (Bi, Sb)₂Te₃ Matrix. *Adv Energy Mater* 2020, **10**: 156-165.
- [6] Acharyya P, Roychowdhury S, Samanta M, *et al.* Ultralow Thermal Conductivity, Enhanced Mechanical Stability, and High Thermoelectric Performance in (GeTe)_{1-2x}(SnSe)_x(SnS)_x. *J Am Chem Soc* 2020, **142**: 20502–20508.
- [7] Bousnina M A, Giovannelli F, Perriere L, *et al.* Ba substitution for enhancement of the thermoelectric properties of LaCoO₃ ceramics (0 ≤ x ≤ 0.75). *J Adv Ceram* 2019, **8**: 519–526.
- [8] Shi X, Ai X, Zhang Q, *et al.* Enhanced thermoelectric properties of hydrothermally synthesized n-type Se&Lu-codoped Bi₂Te₃. *J Adv Ceram* 2020, **9**: 424–431.
- [9] Hanus R, Agne M T, Rettie A J E, *et al.* Lattice Softening Significantly Reduces Thermal Conductivity and Leads to High Thermoelectric Efficiency. *Adv Mater* 2019, **31**: 1–10.
- [10] Tang C, Liang D, Li H, *et al.* Preparation and thermoelectric properties of Cu_{1.8}S/CuSbS₂ composites. *J Adv Ceram* 2019, **8**: 209–217.
- [11] Chen Z G, Shi X, Zhao L D, *et al.* High-performance SnSe thermoelectric materials: Progress and future challenge. *Prog Mater Sci* 2018, **97**: 283–346.
- [12] Zhao L D, Lo S H, Zhang Y, *et al.* Ultralow thermal conductivity and high thermoelectric figure of merit in SnSe crystals. *Nature* 2014, **508**: 373–377.
- [13] Chang C, Wu M, He D, *et al.* 3D charge and 2D phonon transports leading to high out-of-plane ZT in n-type SnSe crystals. *Science* 2018, **360**: 778–783.
- [14] Shi X L, Tao X, Zou J, *et al.* High-Performance Thermoelectric SnSe: Aqueous Synthesis, Innovations, and Challenges. *Adv Sci* 2020, **7**: 25-29.
- [15] Sassi S, Candolfi C, Vaney J B, *et al.* Assessment of the thermoelectric performance of polycrystalline p-type SnSe. *Appl Phys Lett* 2014, **104**: 199-210.

- [16] Ge Z H, Song D, Chong X, *et al.* Boosting the Thermoelectric Performance of (Na, K)-Codoped Polycrystalline SnSe by Synergistic Tailoring of the Band Structure and Atomic-Scale Defect Phonon Scattering. *J Am Chem Soc* 2017, **139**: 9714–9720.
- [17] Zhao L D, Tan G, Hao S, *et al.* Ultrahigh power factor and thermoelectric performance in hole-doped single-crystal SnSe. *Science* 2016, **351**: 141–144.
- [18] Wei W, Chang C, Yang T, *et al.* Achieving High Thermoelectric Figure of Merit in Polycrystalline SnSe via Introducing Sn Vacancies. *J Am Chem Soc* 2018, **140**: 499–505.
- [19] Huang X Q, Chen Y X, Yin M, *et al.* Origin of the enhancement in transport properties on polycrystalline SnSe with compositing two-dimensional material MoSe₂. *Nanotechnology* 2017, **28**: 189–195.
- [20] Naguib M, Kurtoglu M, Presser V, *et al.* Two-dimensional nanocrystals produced by exfoliation of Ti₃AlC₂. *Adv Mater* 2011, **23**: 4248–4253.
- [21] Anasori B, Lukatskaya M R, Gogotsi Y. 2D metal carbides and nitrides (MXenes) for energy storage. *Nat Rev Mater* 2017, **2**:152-159.
- [22] Huang L, Lu J, Ma D, *et al.* Facile: In situ solution synthesis of SnSe/rGO nanocomposites with enhanced thermoelectric performance. *J Mater Chem A* 2020, **8**: 1394–1402.
- [23] Fu Z, Wang N, Legut D, *et al.* Rational Design of Flexible Two-Dimensional MXenes with Multiple Functionalities. *Chem Rev* 2019, **5**: 125-158.
- [24] Fan Y, Jiang W, Kawasaki A. Highly conductive few-layer graphene/Al₂O₃ nanocomposites with tunable charge carrier type. *Adv Funct Mater* 2012, **22**: 3882–3889.
- [25] Ghidui M, Lukatskaya M R, Zhao M Q, *et al.* Conductive two-dimensional titanium carbide clay with high volumetric capacitance. *Nature* 2015, **516**: 78–81.
- [26] Li S, Wang Y, Chen C, *et al.* Heavy Doping by Bromine to Improve the Thermoelectric Properties of n-type Polycrystalline SnSe. *Adv Sci* 2018, **5**: 6–11.
- [27] Shi X, Wu A, Feng T, *et al.* High Thermoelectric Performance in p-type Polycrystalline Cd-doped SnSe Achieved by a Combination of Cation Vacancies and Localized Lattice Engineering. *Adv Energy Mater* 2019, **9**: 1–15.
- [28] Chandra S, Biswas K. Realization of High Thermoelectric Figure of Merit in Solution Synthesized 2D SnSe Nanoplates via Ge Alloying. *J Am Chem Soc* 2019, **141**: 6141–6145.
- [29] Shi G, Kioupakis E. Quasiparticle band structures and thermoelectric transport properties of p-type SnSe. *J Appl Phys* 2015, **117**: 0–10.

[30] Chandra S, Banik A, Biswas K. N-Type Ultrathin Few-layer Nanosheets of Bi Doped SnSe: Synthesis and Thermoelectric Properties. *ACS Energy Lett* 2018, **3**: 1153–1158.

[31] Wei P C, Bhattacharya S, Liu Y F, *et al.* Thermoelectric Figure-of-Merit of Fully Dense Single-Crystalline SnSe. *ACS Omega* 2019, **4**: 5442–5450.

[32] Gholivand H, Fuladi S, Hemmat Z, *et al.* Effect of surface termination on the lattice thermal conductivity of monolayer $Ti_3C_2T_z$ MXenes. *J Appl Phys* 2019, **126**: 125-129.

Figures



Figure 1

Schematic illustration of preparation of SnSe/Ti₃C₂T_x- ω ($\omega = 0, 0.05\%, 0.1\%, 0.2\%$) composites.

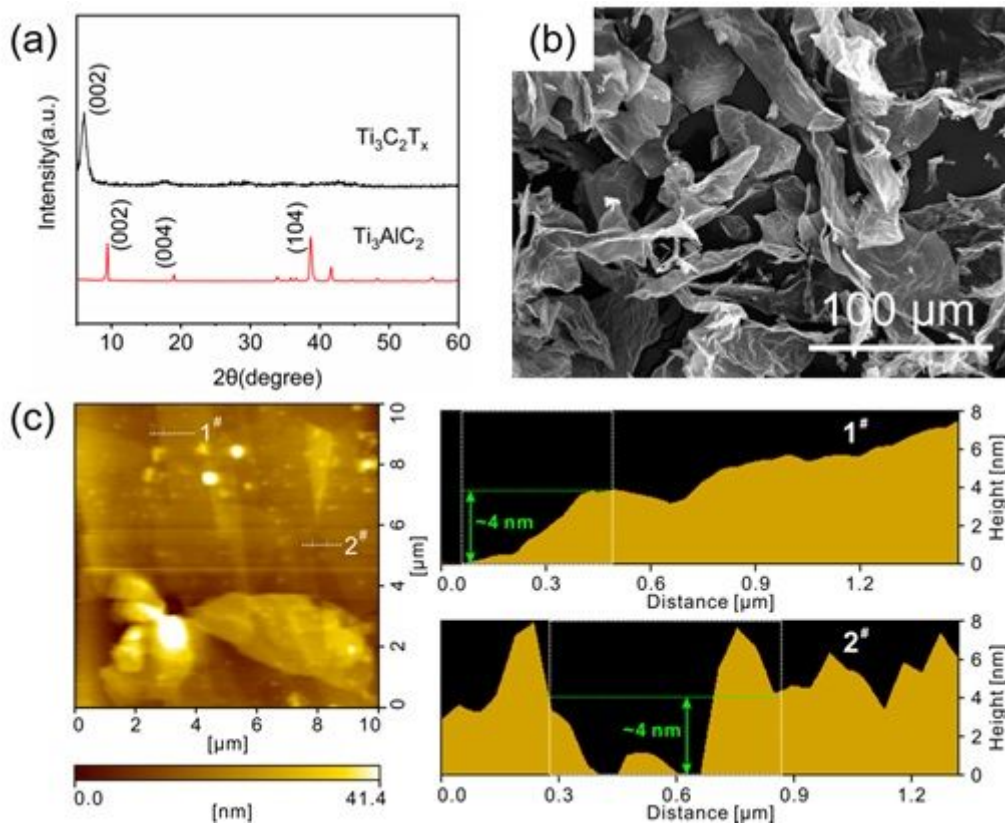


Figure 2

(a) XRD patterns of Ti_3C_2Tx nanosheets. (b) SEM image of Ti_3C_2Tx nanosheets (c) AFM image with a height profile of a Ti_3C_2Tx nanosheet.

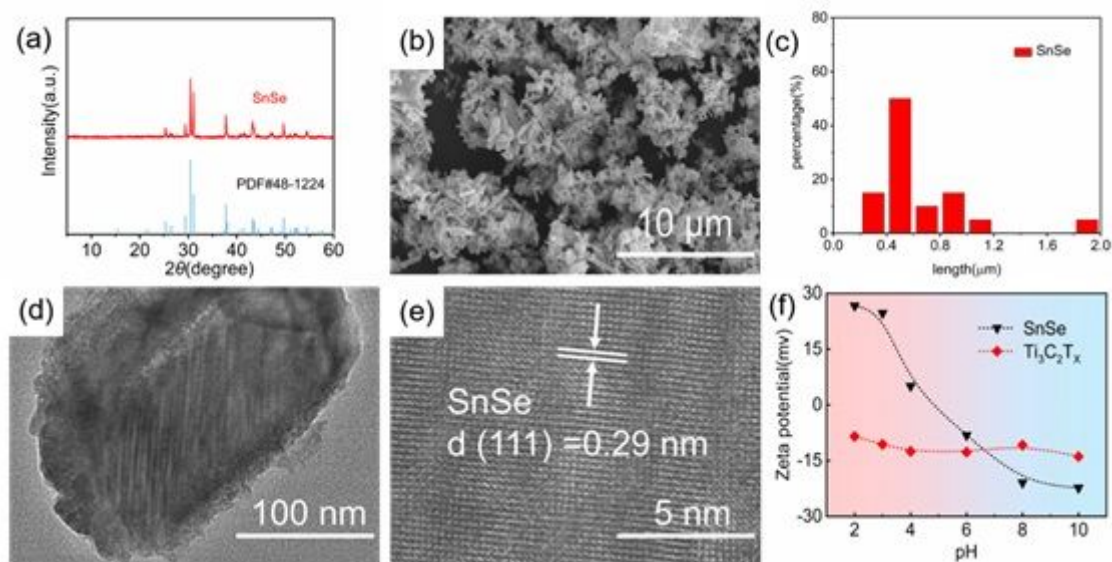


Figure 3

(a) XRD patterns of SnSe. (b) SEM image of SnSe. (c) particle size distribution diagram of SnSe in Fig. 3(b). (d) low-magnification and (e) high-magnification TEM images of SnSe. (f) Zeta potential of Ti_3C_2Tx and SnSe as a function of pH.

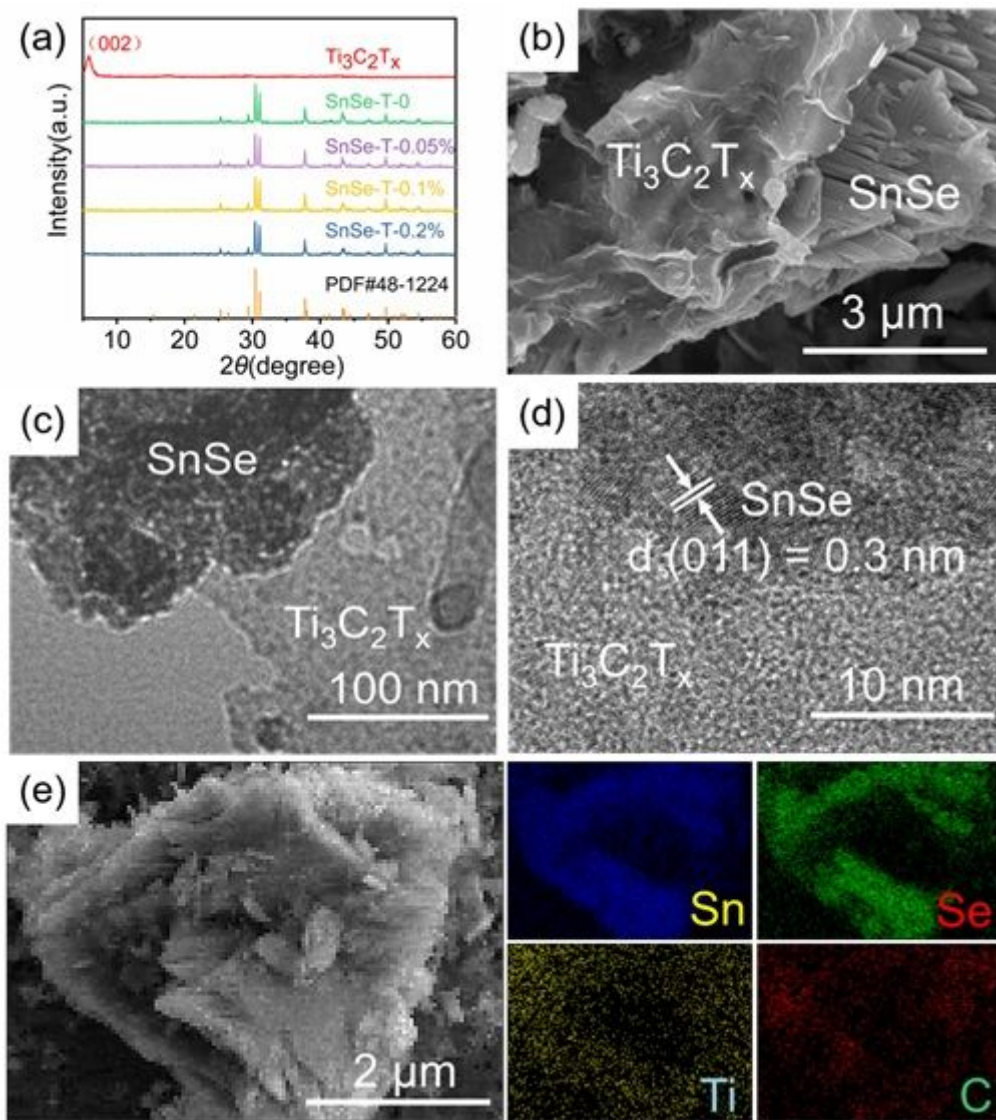


Figure 4

(a) XRD patterns of Ti₃C₂T_x and SnSe/Ti₃C₂T_x composites. (b) SEM image of SnSe/ Ti₃C₂T_x-0.2%. (c) low-magnification and (d) high-magnification TEM images of SnSe/ Ti₃C₂T_x-0.2%. (e) the corresponding elemental maps of Sn, Se, Ti, and C.

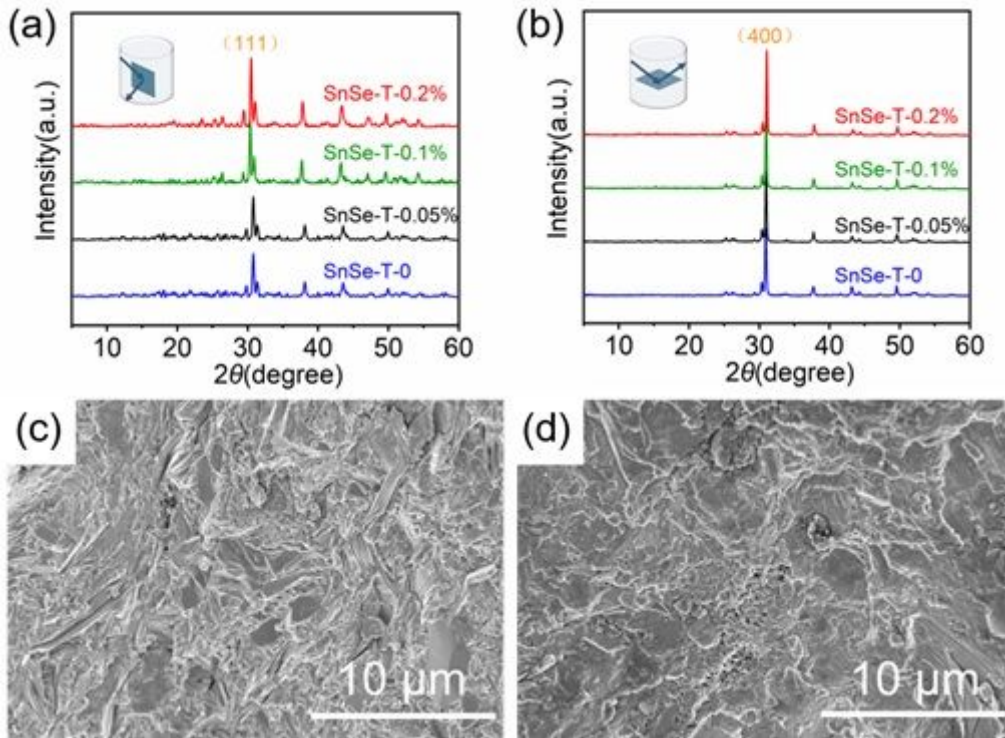


Figure 5

XRD patterns of SnSe/Ti₃C₂T_x composites sintered pellets (a) parallel and (b) perpendicular to the pressing direction. SEM images of SnSe/Ti₃C₂T_x-0.1% pellet fractured from (c) parallel and (d) perpendicular to the pressing direction.

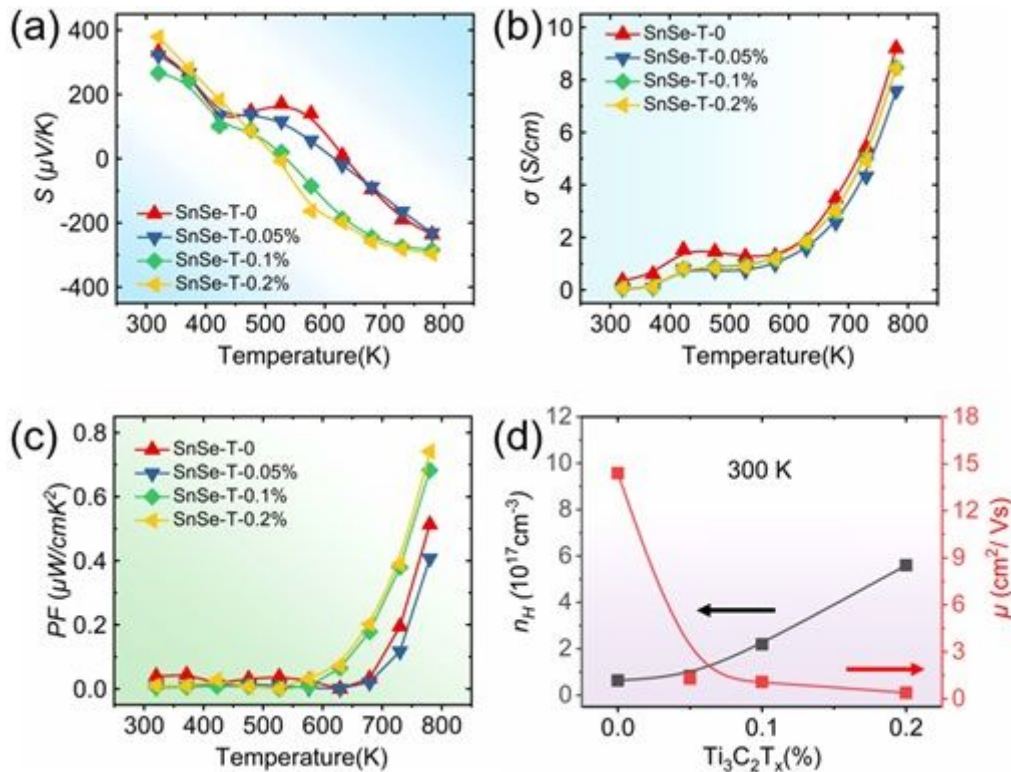


Figure 6

Temperature-dependent electrical properties of SnSe/Ti₃C₂T_x composites measured parallel to the pressing direction. (a) Seebeck coefficient. (b) electrical conductivity. (c) power factor. (d) Hall carrier concentration and carrier mobility as a function of Ti₃C₂T_x mass fraction at room temperature.

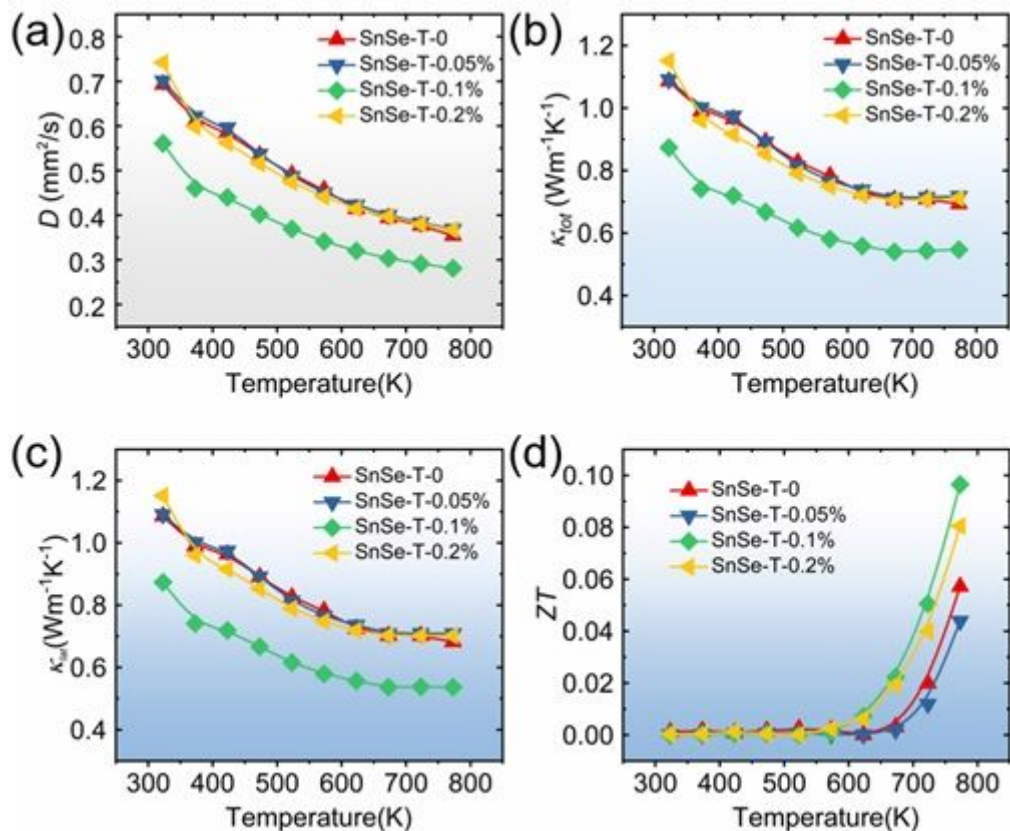


Figure 7

Temperature-dependent (a) thermal diffusion coefficient. (b) total thermal conductivity. (c) lattice thermal conductivity. (d) thermoelectric figure of merit (ZT) of SnSe/Ti₃C₂T_x composites measured parallel to the pressing direction.